Journal of Applied Fluid Mechanics, Vol. 16, No. 9, pp. 1853-1864, 2023.
Available online at www.jafmonline.net, ISSN 1735-3572, EISSN 1735-3645.
https://doi.org/10.47176/jafm.16.09.1813

Influence of External Magnetic Field on 3D Thermocapillary Convective Flow in Various Thin Annular Pools Filled with Silicon Melt

M. O. Azzoug[1], B. Mahfoud[2†], Hibet. E. Mahfoud[3]

[1]*Department of Mechanical, University of UAMO-Bouira, 10000, Algeria*
[2]*Laboratory of Materials and Sustainable Development (LMDD), University of AMO-Bouira, 10000, Algeria*
[3]*Technicum of Collo, Education –Skikda, 21000, Algeria*

†*Corresponding Author Email: b.mahfoud@univ-bouira.dz*

ABSTRACT

Thermocapillary convection flows can have an impact on the homogeneity of floating zone semiconductor crystals. An external magnetic field can also help to reduce this non-homogeneity. The goal of this research is to minimize thermocapillary convection in various thin annular pools filled with silicon melt. A three-dimensional (3D) numerical technique is proposed that employs an implicit finite volume formulation. The steady-state thermocapillary flow in six thin annular pools (R=0.3, 0.4, 0.5, 0.6, 0.7, and 0.8) subjected to an externally induced magnetic field was observed. Under magnetic field influence, the effects of increasing annular gap, *R* on the hydrothermal wave number and azimuthal pattern are obtained. The results reveal that hydrothermal waves *m*=14, *m*=11, *m*=8, *m*=6, *m*=4, and *m*=3 are observed in steady flow for *R*=0.3; 0.4; 0.5; 0.6; 0.7, and R=0.8, respectively. The maximum temperature occurs in the intermediate zone between the inner and outer walls when there is no magnetic field. Under a strong enough magnetic field, isothermal lines change form and become concentric circles. As the amplitude of the magnetic field (Ha) grows, the azimuthal velocity and temperature at the free surface reduce, and the asymmetric 3D flow becomes axisymmetric steady when Ha surpasses a threshold value.

Article History

Received February 8, 2023
Revised April 6, 2023
Accepted April 20, 2023
Available online July 1, 2023

Keywords:

Thermocapillary convection
hydrothermal wave
Magnetic field
Annular pools
Silicon melt

1. INTRODUCTION

Monocrystalline silicon is the base material for computer processors and mobile phones, which are utilized in almost all electronic devices today. Because of its propensity to absorb radiation, monocrystalline silicon is also utilized to create photovoltaic cells in the field of solar energy (Wang et al., 2003). The most common production approach is the Czochralski process, which involves immersing a properly oriented rod-mounted seed crystal in molten silicon (Voronkov, 1982). Simultaneously, thermocapillary convective flows may hurt the homogeneity of floating-zone semiconductor crystals (Okano et al., 1989). Thermocapillary convection occurs in a variety of processes, including crystal formation from melt. The oscillatory melt flow is now known to be a primary cause of the formation of undesirable micro-inhomogeneities in crystals produced from a melt (Mihel & Wingerath, 1987). Thermal boundary conditions have a crucial influence on the displacement of hydrothermal waves according to Li et al. (2004), who studied thermocapillary flow in a shallow circular pool containing molten silicon. A study by Wang et al. (2014) confirmed that heat flux contributes more to melting temperature increases under bidirectional temperature conditions. Then, under the identical settings as the previous investigation, Wang et al. (2015) chose the horizontal direction to execute temperature deference.

The crystallization process under a magnetic field can lessen the strength of the convective flow of silicone melt, reducing oscillatory instabilities in the crystal (Sankar et al., 2011). Several publications dealing with the combination of the magnetic field and mixed or natural convection in closed systems have been made recently, among which is cited (Mahfoud & Bessaih, 2012a, b). An induced current arises when a magnetic field is applied to a flow containing an electrically conductive fluid, according to substantial studies in this area (eg liquid metals or Silicon melt). The induced

Nomenclature

B_0	magnitude of magnetic field, Tesla	***Greek Letters***	
F_M	dimensionless Lorentz force	α	fluid thermal diffusivity
H	height of the cylinder	Θ	dimensionless temperature
Ha	Hartmann number	ν	kinematic viscosity of fluid
J	dimensionless current density	λ	thermal conductivity
P	dimensionless pressure	ρ	fluid density
Pr	Prandtl number	ψ	hydrodynamic streamfunction
R	annular gap	σ	Electric conductivity
r_o, r_i	outer radius, inner radius	α	Thermal diffusivity
r, θ, z	dimensionless spatial coordinates	ε	Emissivity
Re_T	Reynolds number	Φ	dimensionless electric potential
Ma	Marangoni number	***Subscripts and superscripts***	
Ra	Radiation number	c	cold
T_m	melting temperature of silicon	h	hot
V	dimensionless velocity vector		

current interacts with the magnetic field, causing an electromagnetic force (Lorentz force) to be generated that reacts in the opposite direction of the flow (Mahfoud et al., 2016; Mahfoud & Bessih, 2016; Bendjaghlouli, 2019a,b). The flow of liquid metal in a closed cylindrical vessel with a bottom wall that causes eddy flow due to electromagnetic force has become a popular subject of study. In this context researchers like (Sivasankaran et al., 2008; Bhuvaneswari et al., 2011; Sivasankaran et al., 2011, 2017) are interested in industrial applications. Let us consider MHD flows in cavities driven by a lid with corner heating elements in this example (Malleswaran & Sivasankaran, 2016). In addition, the studies carried out by Karthikeyan et al. (2016) and Niranjana et al. (2017) confirm that the mixed convection MHD flow shows that the velocity, and the temperature increase when the parameter of Dufour increases.

In the previous studies, it was confirmed that an external magnetic field can effectively control the flow of liquid metal caused by temperature gradients and rotation in confined media (Mahfoud et al., 2019a,b; Mahfoud & Moussaoui, 2023). The enhanced heat transfer is also improved by using an external magnetic on the swirling nanofluid (Mahfoud & Bendjaghlouli, 2018; Mahfoud, 2023a,b, 2022). The combination between the nanofluid and the magnetic field is also a very interesting subject (Bouragbi et al., 2021; Boulkroune et al., 2021, Slatni et al., 2022). The magnetic field dampens the oscillatory flow, reducing instability and the number of fluid layers, as demonstrated by Benhacine et al. (2021, 2022a,b) on coaxial containers. Mahfoud (2021a,b) examined the impact of various flow structure parameters such as electrical conductivity walls and annulus space. Several studies affirm that a magnetic field may be used to regulate the position and length of a vortex breakdown, as demonstrated by the work of Laouari et al. (2021). Other research focuses earlier on the strong magnetic field effect and its role in the structure of the flow formed in cylindrical and annular containers (Dash, 2017; Dash & Singh, 2019a,b; Dash 2021). Based on this research studied the swirling flow in a cylindrical cavity and annulus under the influence of an axial magnetic field. Another investigation, done by Mahfoud and Hibet (2023), demonstrated that by selecting an appropriate magnetic field intensity, the vortex may be dissipated. It is also found in an article published by Rao and Peng (2017) confirms that the 3D steady flow thermocapillary would transform by a vertically oriented magnetic field into a base flow.

Most Marangoni-thermocapillary debates concentrate on the convection generated by temperature differences, therefore few studies is about controlling this convection. The primary purpose of this research is to employ an external force to guide thermocapillary convection. This force, produced by a magnetic field orientated vertically on the silicon melt pool, aids to suppress the unstable flow. The thin annular geometric is one of the factors that characterize this study. This geometric parameter is crucial in the formation of thermocapillary convection, and its active participation in the industrial manufacture of crystalline materials will be explored.

2. MATHEMATICAL MODEL AND NUMERICAL METHODOLOGY

The thin annular pool filled with silicon melt depicted in Fig. 1 has a thickness of d=3mm, an outer radius of r_o = 50*mm* and an inner radius that corresponds to the six situations investigated here r_i Results of numerical simulations are presented for r_i = 35*mm*; 30*mm; 25mm*, 20*mm*, 15*mm*, and 10*mm* corresponds to six annular gaps R = 0.3, 0.4, 0.5, 0.6, 0.7 and 0.8, in which R=1- (r_i/r_o) . Assuming that T_m is the melting point of silicon, a thermal difference appears between the outer and inner walls of the thin pool when the temperature of the outer solid wall (T_h) is slightly higher than the temperature of the inner solid wall (T_c). Suppose also that T_c equals T_m. A heat flux density q, leads to heating the solid bottom of the pool vertically. Thermal radiation is the main cause of heat dissipation from the upper free surface to the surrounding environment at Ta= 1599K. In addition, the system is subject to a magnetic field that acts axially on the thin pool. Table 1 lists the physical parameters of silicon melt.

2.1 Mathematical Model

The flow is described as laminar, Newtonian and incompressible fluid. At liquid-solid borders, the no-slip criterion is used. The thermocapillary force exerts its

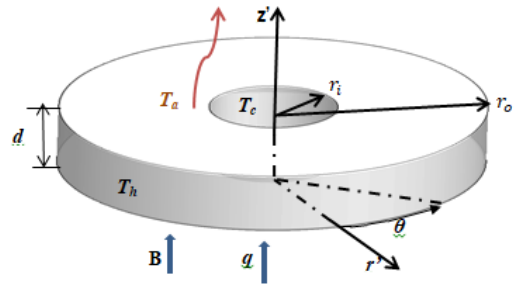

Fig. 1. Flow configuration.

Table 1 Physical properties of silicon melt at T_m = 1683K (Rao & Peng, 2017)

Parameter	value	unit
Density, ρ	2530	kg/m^3
Surface tension coefficient, γ_T	-7.0×10^{-5}	N/(m·K)
Heat capacity, CP	1000	J/(kg·K)
Thermal conductivity, λ	64	W/(m·K)
Viscosity, μ	7.0×10^{-4}	kg/(m·s)
Thermal diffusivity, α	2.53×10^{-5}	m^2/s
Prandtl number, Pr	0.011	-
Emissivity, ε	0.318	-
Magnetic permeability μ_0	1.26×10^{-6}	H/m
Electric conductivity, σ	1.2×10^6	S/m

influence on the free surface, in which is supposed to be non-deformable and flat. The gravity term is ignored in the current work, which has been demonstrated by (Rao & Peng, 2017). An external axial magnetic field, (B_0 $\mathbf{e}_z$), operating in the z-direction is applied to the whole molten silicon and solid walls. Every solid boundary is electrically isolated. The time, length, velocity, pressure, and electric potential are non-dimensionalized by r_o^2/ν, r_o, ν/r_o, $\rho\nu^2/r_o^2$, and $B_0\nu$, respectively. Hence the dimensionless governing equations become:

$$\nabla.\boldsymbol{V} = 0 \tag{1}$$

$$\frac{\partial \boldsymbol{V}}{\partial t} + \boldsymbol{V}.\nabla\boldsymbol{V} = -\nabla P + \nabla^2\boldsymbol{V} + \boldsymbol{F}_M \tag{2}$$

$$\frac{\partial \Theta}{\partial \tau} + \boldsymbol{V}.\nabla\Theta = \frac{1}{\mathrm{Pr}}\nabla^2\Theta \tag{3}$$

The presence of a magnetic field results in the presence of a force acting on the moving electric charges (known as the Lorentz force). The Lorentz force $\boldsymbol{F}_M$ is just a function of r and θ, which may be

calculated as follows:

$$\nabla^2\Phi = \nabla.(\mathrm{U} \times \boldsymbol{e_z}) \tag{4}$$

$$\boldsymbol{J} = -\nabla\Phi + (\mathrm{U} \times \boldsymbol{e_z}) \tag{5}$$

$$\boldsymbol{F}_M = \vec{\boldsymbol{J}} X \vec{\boldsymbol{B}} = \frac{1}{\mu_0}(\nabla \times \vec{\boldsymbol{B}}) \times \vec{\boldsymbol{B}} \tag{6}$$

Here, $\Theta = T/T_c$ is the dimensionless temperature. The non-dimensional electric potential and pressure were designed by Φ, and P. $\mathbf{V}$ is the velocity vector, and the unit vector ($\mathbf{e}_z$) is oriented in the axial direction.

At the upper free surface, the boundaries are:

$(z = d/r_o,\ r_i/r_o \le r \le 1,\ 0 \le \theta < 2\pi)$:

$$\frac{\partial u}{\partial z} = Re_T\frac{\partial \Theta}{\partial r},\ \frac{\partial w}{\partial z} = Re_T\frac{1}{r}\frac{\partial \Theta}{\partial r},\ w = 0,$$

$$\frac{\partial \Theta}{\partial z} = -R_{ad}(\Theta^4 - {\Theta_a}^4);\quad \frac{\partial \Phi}{\partial z} = 0,$$

At the solid bottom

$(z = 0,\ r_i/r_o \le r \le 1\ , 0 \le \theta \le 2\pi)$:

$$u = v = w = 0, \frac{\partial \Theta}{\partial z} = -Q\ , \frac{\partial \Phi}{\partial z} = 0\ ;$$

At the inner wall

$(0 \le z \le d/r_o\ , r = r_i/r_o\ , 0 \le \theta \le 2\pi)$:

$$u = v = w = 0, = 0\ , \Theta = 1,\ \frac{\partial \Phi}{\partial z} = 0\ ;$$

At the outer wall

$(0 \le z \le d/r_o\ ,\ r = 1,\ 0 \le \theta < 2\pi)$:

$$u = v = w = 0, \Theta = T_h/T_c\ , \frac{\partial \Phi}{\partial Z} = 0\ ;$$

The Stokes function (non-dimensional stream function) ψ is defined in cylindrical coordinates by $v = \partial\psi/(r\partial r),\ u = -\partial\psi/(r\partial z)$.

In the above equations Q and γ_T, Re_T, R_{ad} and Pr are, respectively, non-dimensional heat flux, Temperature coefficient of the surface tension, thermocapillary Reynolds number, radiation number and the Prandtl number which are defined as:

$$\begin{cases} Q = qr_o/(\lambda T_c) \\ \gamma_T = -\partial\gamma/\partial T \\ Re_T = -\gamma_T\ T_c r_o/\mu\nu \\ R_{ad} = \varepsilon\sigma\ (T_h - T_c)^3\ r_o/\lambda \\ Pr = \nu/\alpha \end{cases} \tag{7}$$

The Hartmann number $(Ha = B_0 r_o\sqrt{\sigma/(\rho\nu)})$ signifies the proportion of electromagnetic force to viscous force. $Ma = -\gamma_T\ (T_h - T_c) r_o/\mu\alpha$ is the Marangoni number, which gives the ratio between the thermocapillary effect and the viscous forces.

2.2. Numerical Solution and Grid Sizes.

The finite volume approach is used to discretize the equations, and the PISO algorithm is used to solve them. The diffusion components are computed using a second-order central difference scheme, whereas the convective terms are computed using a higher-order differencing method (QUICK). The pressure-velocity coupling is solved by the SIMPLER algorithm (Patankar, 1980).

Current simulations use a fine mesh, taking into account the Hartmann thickness (~ Ha^{-1}) and Roberts layers (~ $Ha^{-2/3}$), which require refinement near the walls. A non-uniform staggered grid arrangement in the radial and axial axes is used here. Regular grids have been used in the azimuth direction (Table 2).

Table 2 Grid sizes selected

Annular gap	Mesh(n_r, n_θ, n_z)
R=0.3	35×110×30
R=0.4	45×110×30
R=0.5	55×110×30
R=0.6	75×110×30
R=0.7	85×110×30
R=0.8	95×110×30

Several grids were investigated to produce a grid-independent solution, and the best grid was chosen. To maintain good precision, the grid must be carefully chosen while considering the change in annular space. To that purpose, two cases with predicted maximum temperature gradients and velocities were chosen, and the mesh-independence analysis was performed on them.

As a result, in the absence of a magnetic field, the cases which have an annulus *R*=0.5 and *R*=0.7 was tested. Attempts were made at first to identify the ideal amount of meshes (see Fig. 2). The dimensionless azimuthal velocity on the radial line on the free surface of the annulus (z =H) was compared for three different grids after identifying the appropriate number of meshes in the grid for different directions.

As shown for case R=0.7 in Fig. 2a, the differences in the results of 85×110×30 and 90×120×35 are negligible, and, hence, the grid of 85×110×30 was determined to be acceptable for this choice. In the same way, the grid of 55×110×30 was chosen in the case of R=0.5 (Fig 2b). In the same procedure for the other cases, appropriate grids about the dimensions were used.

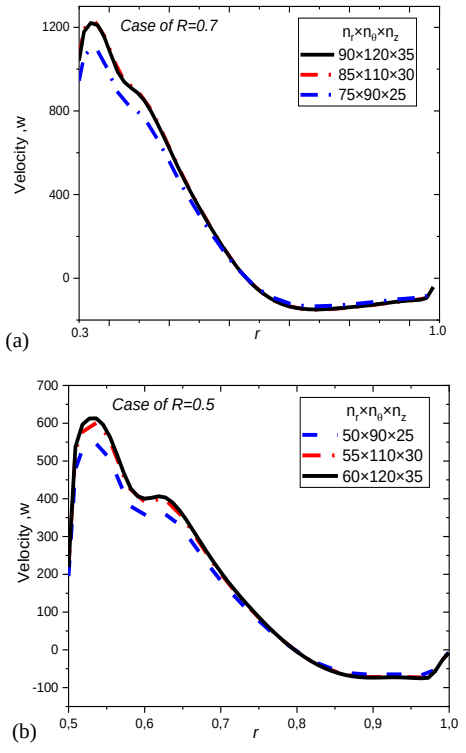

Fig. 2. Profiles of w velocity for different grids (a) *R*=0.7 and (b) *R* =0.5.

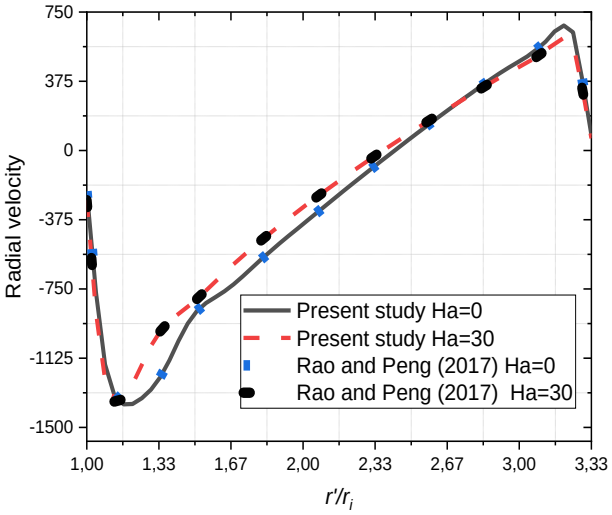

Fig. 3. Radial profile of radial velocity: present result compared with Rao and Peng (2017).

Numerical simulations were performed at Bouira University's Computer Center using an HP Z8 G4 Workstation (128 GB). Convergence was assumed at each time step if the maximum residual error of the continuity equation between all control volumes was less than 10^5. The time step was chosen to be somewhere between 10^{-3} and 10^{-4} seconds.

3. RESULTS AND DISCUSSION

3.1. Validation

First, these results obtained are validated with the numerical results found by Rao and Peng (2017). The comparison of the apportionment of radial velocity under increasing magnetic field on a free surface at θ= 0 is shown in Fig.3. When the heat flow is Q = 4.87 10^{-3}, the comparison of the radial velocity distribution in the case of bidirectional temperature gradients is ΔT = 6K and Marangoni condition (Ma = 356). Two radial velocity profiles are juxtaposed, one depicting the case without a magnetic field (Ha=0) and the other one with a magnetic field (Ha=30). There was an identical agreement in the compared findings.

For the same conditions (Ma = 356, and Q = 4.87 10^{-3}, and ΔT = 6K, the code was then double-checked with Rao and Peng (2017) by comparing the distribution of isothermal contours on the free surface. The results were obtained for two values (Ha = 0 and Ha = 30).

At Ha=30, the flow becomes steady and axisymmetric, but when Ha=0, it is asymmetrical. This is proven by isothermal lines that develop around the inner wall, which have become concentric circles at Ha = 30. Knowing that the initial shape at Ha=0 was squares centered around the inner wall. This comparison yields the same result, indicating that the temperature reduction is small, ranging from Θ=1.005931 when Ha=0 to Θ=1.005792 when Ha=30. The current results, which are shown in Fig.4, are consistent with theirs.

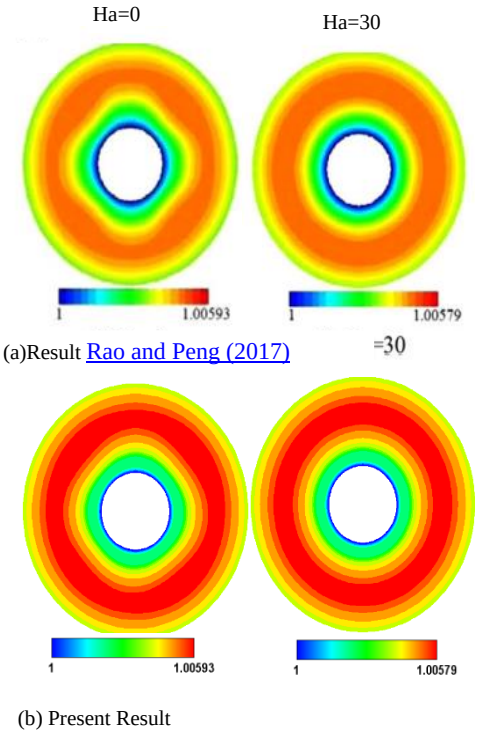

(a)Result Rao and Peng (2017)

(b) Present Result

Fig. 4. Second comparison with Rao and Peng (2017), which presents the distribution of free surface temperature under two values of Ha.

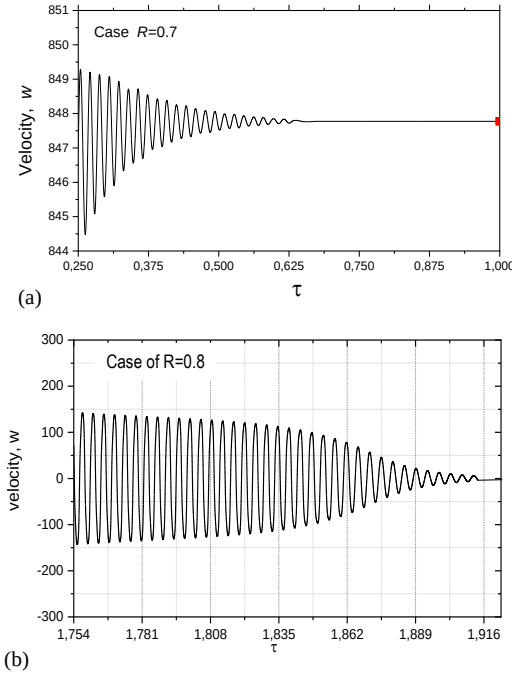

Fig. 5. Temporal evolution of azimuthal velocity for case (a) *R*=0.7 and (b) *R*=0. 8 located at *r* = 0.4 and θ = 30° on the free surface.

3.2. Effect of Annular Gap on Thermocapillary Flow

Results of numerical simulations of steady-state flow are presented for six annular gaps *R* =0.3, 0.4, 0.5, 0.6, 0.7, and 0.8. In all the cases studied here, the heat flux is fixed at q = 3.51W/cm^3, and ΔT = 6K. Likewise, the crystallization temperature (T_c=1683 K) is higher than the minimum melting temperature. Taking the ambient temperature T_a= 1599K at the free surface, and Ma = 1186, for these conditions the molten silicon remains in a stable state for all the annuli, which will be demonstrated in the next paragraph. The resultant high-velocity flow across the gaps R=0.7 and R=0.8 will cause a maybe transient loading which is difficult to predict. For the cases of R=0.7 and R=0.8, a series of numerical computations are done to determine the flow regime, i.e. transient or steady-state. Figure 5 shows the temporal evolutions of azimuthal velocity recorded on the free surface at the point (θ = 30° and *r* = 0.4). For annular gap *R*= 0.7, and also R=0.8, the simulation shows that after a certain oscillation, the flow stabilizes and becomes a steady state. The temporal evolution of *w* shows that the 3D stationary flow remains predominant, where the amplitude of *w* for *R*=0.8 increases compared to the case *R*=0.7(Fig. 5a). This result confirms that the other cases also represent a permanent regime Figure 5 compared the hydrothermal wave number (*m*) which is shown with azimuthal velocity distributions on the top free surface (Fig. 5). This later propagates in the radial thermocapillary direction due to the combined impact of ΔT and Q. Standing waves form around the inner and outer walls as a result of the counter-rotating convection cells created by this combined impact.

Figure 6(a) shows simulation results for *R*=0.3, in this case the wave number is about *m*=14. The combined temperature gradient and heat flow generated fourteen standing waves. The maximum non-dimensional azimuthal velocity is about w_{max}=120. The contours of temperature forms on the free surface are similar to the azimuthal velocity distribution, where it shows fourteen peaks (Fig. 7a).

The temperature increases monotonically from the inside to the external wall, as seen in Figs 7a-8a. The temperature decreases down the Z axis, with the highest value (Θ= 1.00388) appearing on the bottom and the lowest temperature appearing on the free surface towards the inner wall. Due to the interaction between the flow below as well as the radiating surface above.

Figure 6(b) presents the case when annular gap is *R*=0.4, here the combined influence of temperature gradient and heat flow generated eleven standing waves (*m*=11) which are caused by counter-rotating convection cells. In this case the maximum non-dimensional azimuthal velocity increase to w_{max}=360. It is obvious that the highest temperature is found in the emerging zone at the center of the basin, while a maximum open surface temperature is 1.0034 (see, Fig. 7b). The maximum temperature Θ=1.0041 emerges in the middle region (Fig. 7b), and then decreases as one moves from the central region to the exterior boundaries.

Figure 6(c) shows the case of *R*=0.5 by the contours plot of azimuthal velocity traced on the free surface. In this event, w_{max} rises to 621 in contrast to the preceding case, and the wave number falls even more to *m*=8. The temperature distribution forms on the free surface have eight peaks, that are spaced at regular intervals of θ=45°, also the temperature fluctuation on the free surface increases greatly to Θ=1.00369 (Fig. 7c). The

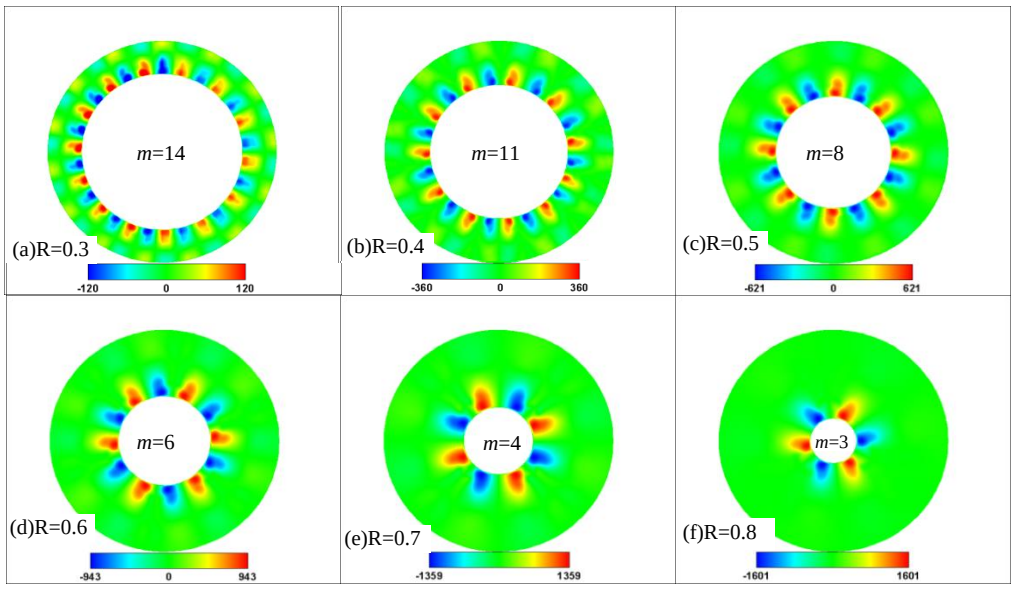

Fig. 6. Distribution of azimuthal velocity on the free surface for the different annular gaps when Ha=0.

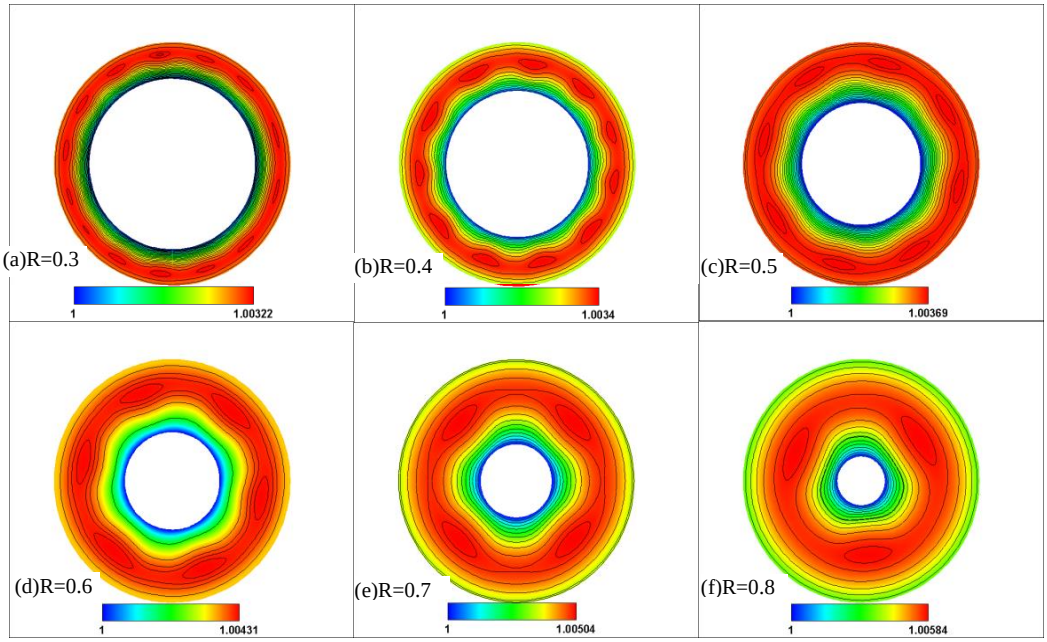

Fig. 7. Distribution of temperature on the free surface for the different annular gaps when Ha=0.

same observation which indicates that in the middle region emerges the maximum temperature (Θ=1.0059). On the other hand on the free surface it is worth Θ=1.00458 (Fig. 8c) .

Figure 6(d) shows the case of R=0.6, the circumferential flows by the azimuthal velocity, it is found six hydrothermal waves (m=6) propagate between the inner cold wall and the hot outer wall. The flow patterns of w show that the 3D stationary flow remains predominant. The w_{max} increases compared to the previous case and becomes 943, which is influenced by counter-rotating convection. The temperature distribution includes six peaks that are spaced at regular intervals of θ=60° (Fig. 7d). On the free surface the maximum temperature is Θ=1.00431, which occurs in the six peaks in the center area, while the maxi temperature emerges in the middle of pool which is Θ=1.00521 (Fig. 8d).

Figure 6(e) shows the case of R=0.7, in which the dimensionless azimuthal velocity on the free surface shows four hydrothermal waves. Here the number of waves generated by counter-rotating convection cells decreases further and becomes m=4. The maximum of w rises sharply to 1359. The temperature fluctuation on the free surface increases sharply, reaching Θ =1.00504 as seen in Fig. 7 (e). But in the median of the pool, the maximum temperature is Θ =1.00593(Fig. 8e). while the high-temperature values have shifted towards the annular pool's center.

Figure 6(f) displays the case of R=0.8, here the thermocapillary flow is characterized by three wave numbers (m=3). The maximum circumferential velocity increases to 1601. So, temperature distribution represents three peaks (Θ =1.00584), which corresponds to a maximum temperature on the free surface (Fig. 7f). The maximum iso-surface temperature merges in the middle of the pool, reaching Θ_{max} =1.0062 (Fig. 8f).

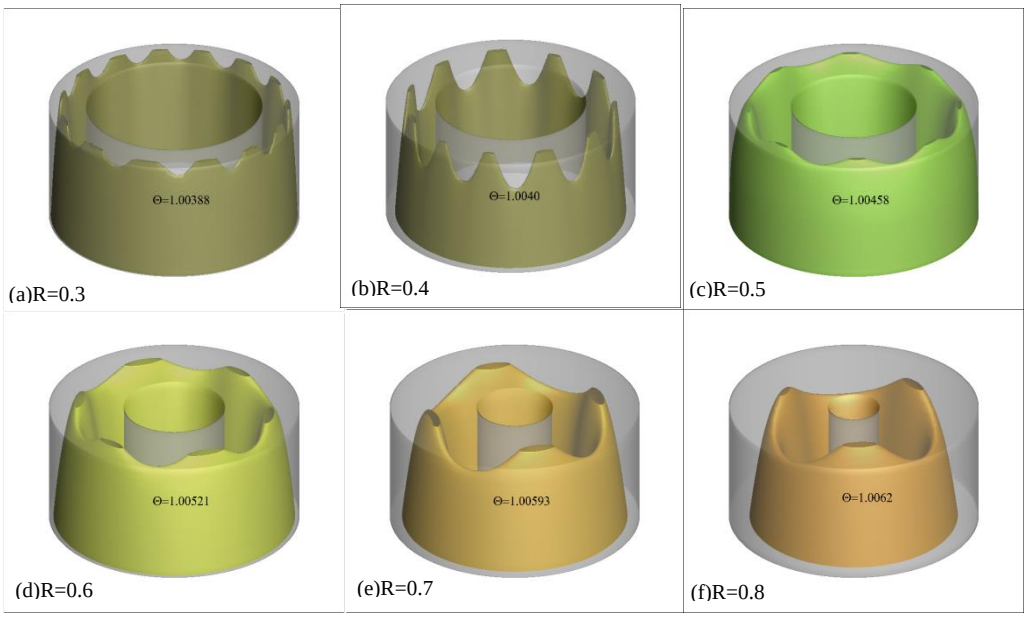

Fig. 8. Iso-surfaces of dimensionless temperature Θ related to the mode *m* =14, 11, 8, 6,4, and 3 corresponding to annular gaps *R*=0.3, 0.4, 0.5, 0.6, 0.7 and 0.8, respectively.

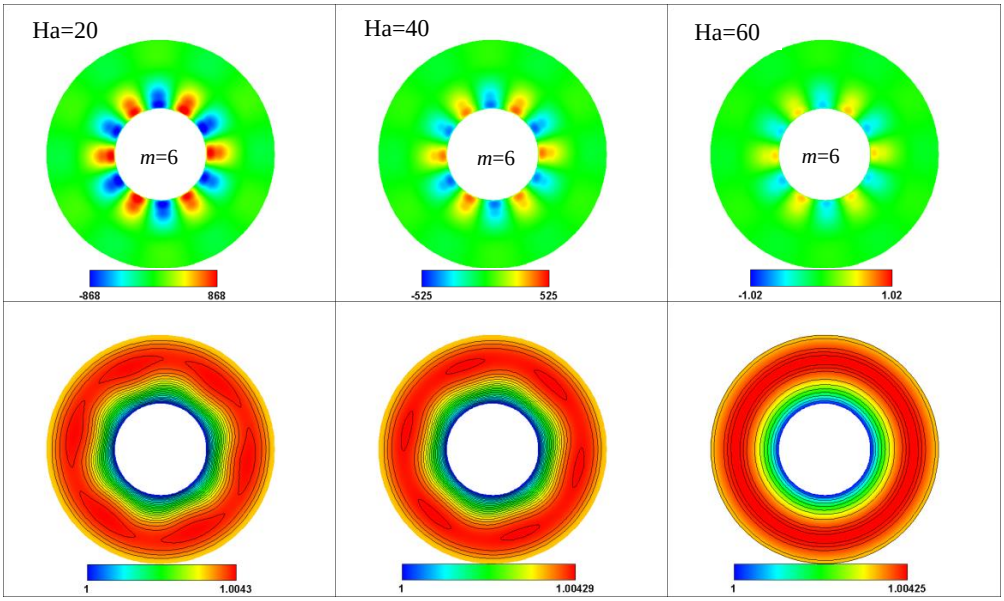

Fig. 9. Effect of magnetic field on the free surface distribution of azimuthal velocity(top), isotherms(below) in case of *R*=0.6.

3.3. Magnetic Field Effect on Velocity and Temperature Distributions

According to previous research, applying a magnetic field enhances the shift from an oscillatory flow to a stable flow, a process known as electromagnetic stabilization. In MHD, an electric potential is created with a new force and following Ohm's law, so that the electric field $\vec{E}$= - $\vec{\nabla}\phi$ opposes the electromotive field. Above all, the velocity profile is significantly altered since the Laplace force is negative in the middle and positive in the Hartmann layer. In this layer formed near the walls, the breaking of the flow by the magnetic field is moderate.

Figures 9-10 displays a series of simulations that were performed for *R*=0.6 and R=0.7, respectively to better understand the increasing effect of *Ha* on the hydrodynamic and isotherms. The value of the dimensionless azimuthal velocity reduces rapidly as the Hartmann number grows, showing that the flow is damped by the created Lorentz force. However, there is no notable variance in the distribution of velocity vectors, implying that the wave numbers *m*=6 for *R*=0.6 and *m*=4 for *R*=0.7 are always dominant. The flow is propelled by the thermocapillary force, which is proportional to the heat source's flux and the temperature gradient. The molten silicon acts as a damper because it flows in the opposite direction of the Lorentz force. With

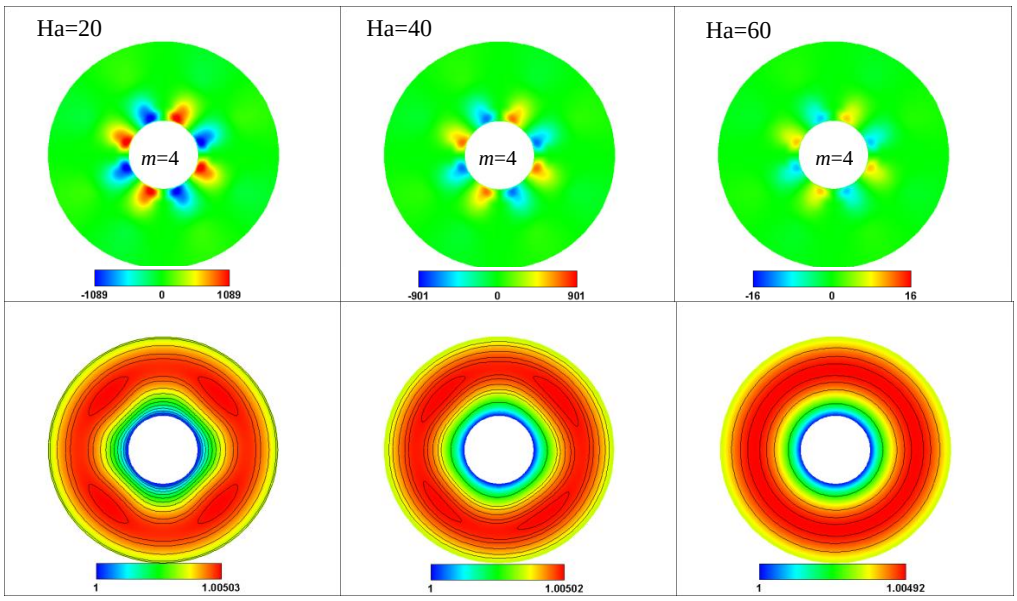

Fig.10. Effect of magnetic field on the free surface distribution of azimuthal velocity(top), isotherms(below) in case of *R*=0.7.

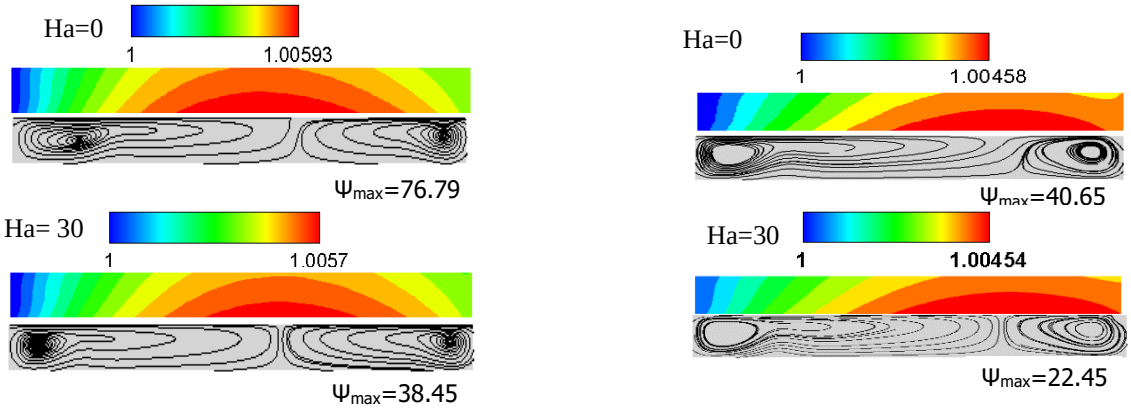

(a) Case R=0.7 (b) Case R=0.5

Fig. 11. Plots of isothermal contours (above), and streamlines (below) on the vertical median plane for Ha=0 and Ha=30.

an increase in the number of Hartmann, the suppressive impact of electromagnetic force is intensified, resulting in stronger confinement of the flow, which results in a decrease in the circumferential velocity. When the Ha rise, the azimuthal velocity on the horizontal free surface reduces on the other side (Fig. 9), as seen by the maximum azimuthal velocity on the free surface, which fell from w_{max}=868.1 for Ha=20 to w_{max}=1.021 for Ha=60 for R=0.6. The same scenario has been observed for R=0.7 (Fig. 9), where w_{max}= 1356.1 for Ha=0 and becomes 16.2 for Ha=60. The decrease in temperature with the increase in Ha is very weak contrary to velocity which decreases rapidly. This is shown in Figs. 9 and 10(lower frame) where the isotherms for the cases Ha = 20, 40, and 60 are compared. It seems that the effect of the increase in the Hartmann value on the temperature is modest compared to its strong effect on the azimuthal velocity. So, in case *R*=0.6 Θ_{max}= 1.0043 for Ha=20 rise to Θ_{max}=1.00425 for Ha= 60.

Also, when *R*=0.7, the same previous note, in which the temperature decreases along the z-axis and the total value in the container decreases from Θ_{max}=1.00503 for Ha=20 to Θ_{max}=1.00492 for Ha= 60. The isothermal contours near the inner cylinder resemble square for R=0.7 and hexagonal for *R*=0.6, whereas those near the outside cylinder resemble circular patterns. When Ha = 60, the distribution of the peaks in temperature on the upper plat surface vanished and was replaced by concentric circles.

The distribution of isothermal contours (above) and streamlines (below) on the median plane for two values (Ha = 0 and Ha = 30) is shown in Fig. 11. In two examples, R=0.7 and R=0.5, the isothermal contours do not vary significantly as *Ha* increases. Yet, if *Ha* rises, the dimensionless stream function falls dramatically. This proves that electromagnetic force in the opposite direction of flow can also be implemented to modify the molten masses of silicon.

For three values of the Hartmann number (Ha=0, 20, and 40), Fig. 12 depicts the radial profiles of azimuthal velocity and temperature drawn on the line that passes through θ = 0 and is positioned on the free surface. As indicated previously, the flow is asymmetrical for *R*=

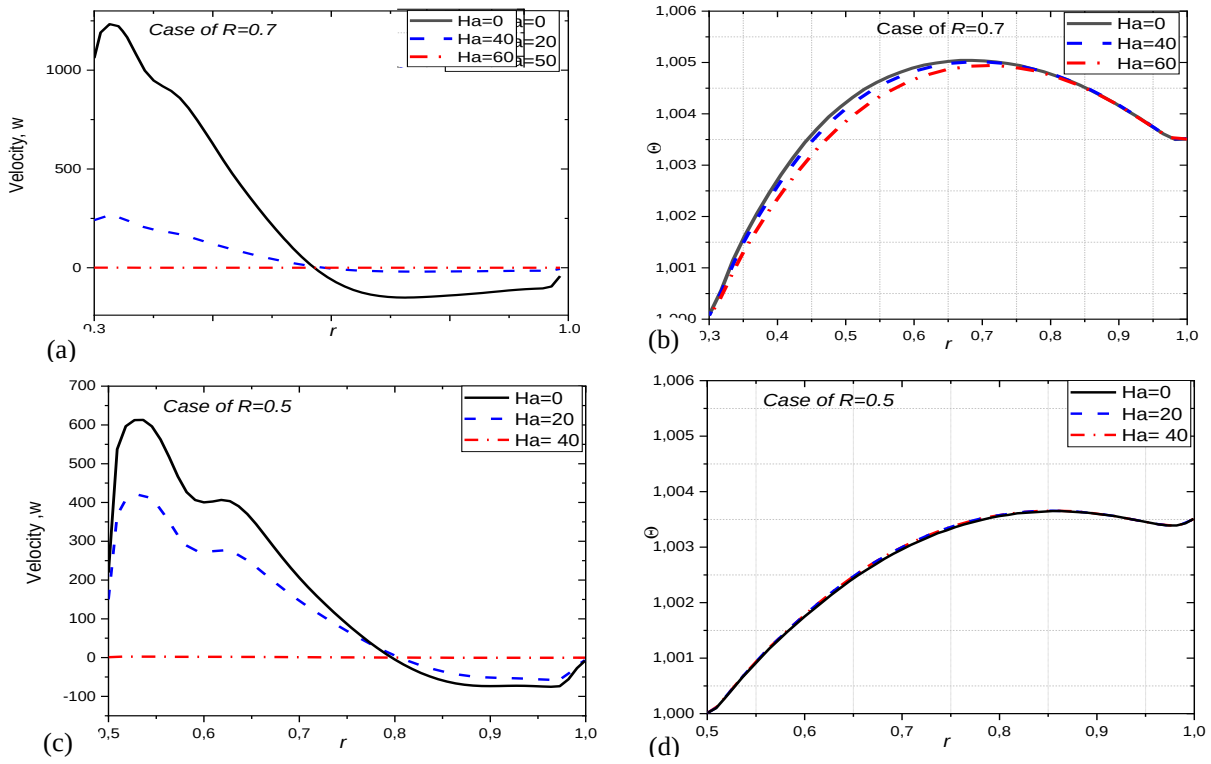

Fig. 12. Radial profiles of the azimuthal velocity and temperature on the free surface at θ =0 at for *R*=0.7 and *R*=0.5 shown at different Hartmann numbers.

0.7 (Fig. 12a). When a magnetic field is added, the flow in asymmetric form is damped and reaches the axisymmetric form, called base flow when *Ha* exceeds a critical value.

The maximum azimuthal velocity for Ha=0 appears at *r*=0.35 which is 1255 (Fig. 12a). When Ha=50, the azimuthal velocity profile becomes almost straight and equals *w*=0. However, this stabilizing effect is due to the Hartmann layer which increases with the magnetic field and gradually replaces the viscous forces. Well, it causes a balance between electromagnetic and viscous forces.

Figure 12b shows radial profiles of the temperature on the free surface at different Hartmann numbers for case R=0.7. For Ha = 0, the temperature reaches the peak at *r* = 0.7, which is Θ =1.00501. After that, it diminishes until Θ =1.0035 at *r*=1.0. When Ha = 40, the behaviors are virtually identical to those without a magnetic influence. When Ha = 50, the temperature, reaches a much smaller peak, Θ=1.00495 at r=0.7 and diminishes slowly to Θ =1.0035. These data demonstrate that the influence of the magnetic force on the temperature field does not have substantial effects. The electromagnetic force, on the other hand, causes a significant modification in the velocity field. Fig. 12(c,d) shows radial profiles of azimuthal velocity on the free surface along the r-axis versus Ha for case *R*=0.5. A similar finding has been made about the inhibitory impact of magnetic force, although in this instance, a large amplitude is not required to create an axisymmetric flow.

The iso-potential contours plotted on the free surface are shown for both numbers (Ha=10 and Ha=50) of Fig. 13.

The induced current, denoted by $\mathbf{J} = -\nabla\Phi + \mathbf{U}\times\mathbf{e}_z$ is divided into two portions. The interaction between silicon melt and the magnetic field $\boldsymbol{B}$ produces the directly induced current, $\mathbf{J}_1 = \mathrm{U}\times\mathrm{e}_z$. The second portion, $\mathbf{J}_2 = -\nabla\Phi$, is caused by the electric potential field. $\mathbf{J}_2$ will frequently form current loops in zones where $\mathbf{J}_1$ is modest because it ensures current conservation, especially for electrically insulating facades in which current conservation must take place inside the liquid. Electric potential is thought to be more essential in electrically insulating walls than in conductive walls. Because current may pass through the walls in this situation, flow damping should be less critical. (Laouari et al., 2021). Finally, when the azimuthal velocity is low on the free face, the maximum electric potential is similarly low. Also, the increase in the annular spaces leads to an increase in the maximum value of the electric potential

4. CONCLUSION

Numerical simulations with 3D were used to examine the thermocapillary process of steady silicon melt flow under a magnetic field. Also observed is the influence of various annular gaps in thin pools filled with silicon melt on the formation of hydrothermal waves. The transport equations were numerically solved resort to the finite-volume approach. The results of the simulation lead to the following conclusions:

- The findings show that for *R*=0.3; 0.4; 0.5; 0.6; 0.7, and R=0.8, hydrothermal waves m=14, m=11, m=8, m=6, m=4, and m=3 develop in steady flow.

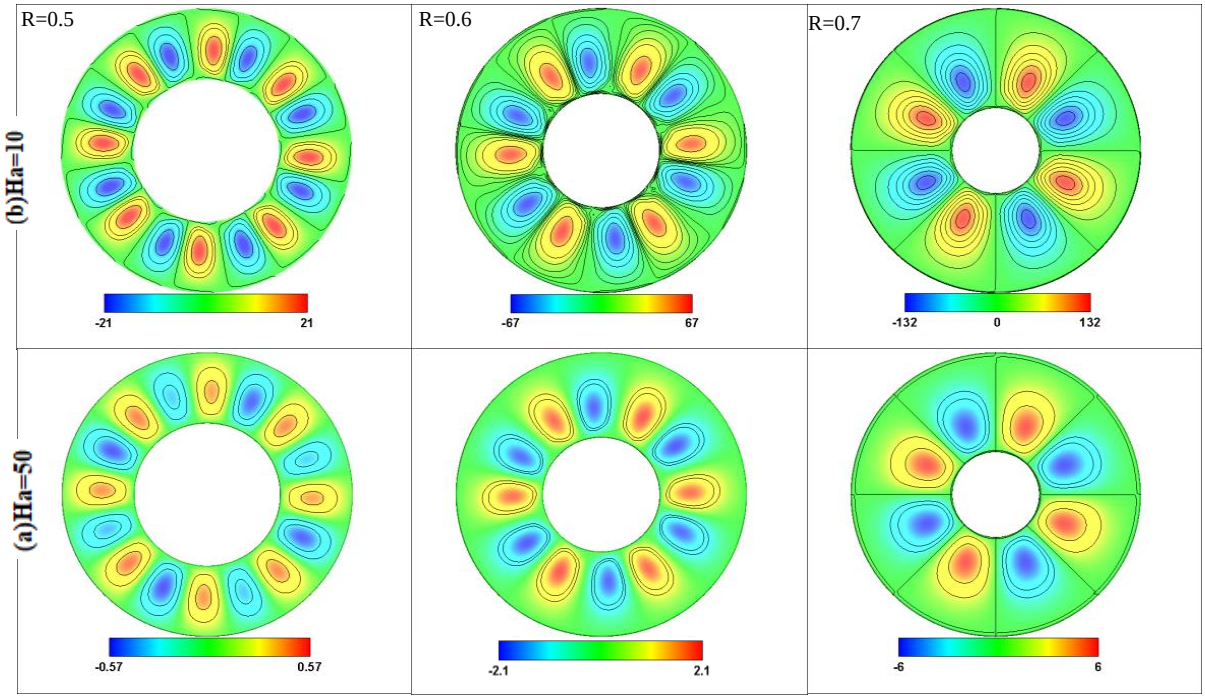

Fig. 13. Effect of magnetic field (Ha=10 and Ha=50) on the free surface distribution of iso-potential in different cases (R=0.5, R=0.6, and R=0.7).

- Without a magnetic field, The vertical heat flow gets priority. The maximum temperature is seen in the zone between both the inner and exterior walls.
- When a strong enough magnetic field is applied to the free surface, the isothermal lines convert into concentric circles.
- As magnetic field amplitude (Ha) increases, the azimuthal velocity decreases, which helps asymmetric 3D flow will become steady axisymmetric when *Ha* exceeds a certain value.
- The observed effect of the magnetic field demonstrates its suitability for use in suppressing thermocapillary convection and getting high quality during the crystallization process.
- Further research using a magnetic field and electrically conductive walls may soon improve crystal production with molten silicon.

ACKNOWLEDGMENTS

The authors gratefully acknowledge the support of the General Directorate of Scientific Research and Technological Development (DGRSDT - Algeria).

CONFLICT OF INTEREST

The authors declare that they have no conflict of interest.

AUTHORS CONTRIBUTION

M. O. Azzoug : Numerical simulations; visualization; review and editing; B. Mahfoud : Supervision, Numerical simulations, writing the original draft, reviewing, and editing, Hibet. E. Mahfoud : review and editing.

REFERENCES

Bendjaghlouli, A., Mahfoud, B., & Ameziani, D. E. (2019a). Magnetohydrodynamic flow in a truncated conical enclosure, *Journal of Thermal Engineering*, 5, 77-83. https://doi.org/10.18186/thermal.532133

Bendjaghlouli, A., Ameziani, D. E., Mahfoud B., & Bouragbi, L. (2019b). Magnetohydrodynamic counter rotating flow and heat transfer in a truncated conical container, *Journal Thermophysics and Heat Transfer*,865-874. https://doi.org/10.2514/1.T5529

Benhacine, H., Mahfoud, B., & Salmi, M. (2021). Stability effect of an axial magnetic field on fluid flow bifurcation between coaxial cylinders, *International Journal of Computational Materials Science and Engineering* 10, 2150023. https://doi.org/10.1142/S2047684121500238

Benhacine, H., Mahfoud, B., & Salmi, M. (2022a). Stability of an Electrically Conducting Fluid Flow between Coaxial Cylinders under Magnetic field. *Journal of Applied Fluid Mechanics* 15, 1741-1753. https://doi.org/10.47176/JAFM.15.02.33050

Benhacine, H., Mahfoud, B., & Salmi, M. (2022b). Stability of conducting fluid flow between coaxial cylinders under thermal gradient and axial magnetic Field. *International Journal of Thermofluid Science and Technology*, 9, 090202. https://doi.org/10.36963/IJTST.2022090202

Bhuvaneswari, M., Sivasankaran, S., & Kim, Y. J. (2011). Magnetoconvection in a square enclosure

with sinusoidal temperature distributions on both side walls, *Numerical Heat Transfer, Part A: Applications*, 59 (3), 167-184. https://doi.org/10.1080/10407782.2011.541219

Boulkroune S., Kholai, O., & Mahfoud, B. (2021). Effects of Important Parameters on the transition from forced to mixed convection flow in a square cavite, *Defect and Diffusion Forum*, 406, 36-52. https://doi.org/10.1142/S2047684121500238

Bouragbi L., Salaheddine, A., & Mahfoud, B. (2021). Analyses of entropy generation for a solar minichannel flat plate collector system using different types of nanofluids, *Journal of Computational Applied Mechanics*, 52(4), 664-681. https://doi.org/10.22059/jcamech.2021.333705.66

Dash, S. C. (2021). MHD braking and joules heating effect in a rotating confined cylindrical cavity packed with liquid metal, *FME Transactions*, 49(2),437-444. https://doi:10.5937/fme2102437D

Dash, S. C. (2017). Study of axisymmetric nature in 3-d swirling flow in a cylindrical annulus with a top rotating lid under the influence of axial temperature gradient or axial magnetic field, *Journal of Thermal Engineering*, 3(6), 1588-1606. https://doi.org/10.18186/journal-of-thermal-engineering.353737

Dash, S. C., & Singh, N. (2019a). Effect of a strong axial magnetic field on swirling flow in a cylindrical cavity with a top rotating lid, *International Journal of Modern Physics C*, 30(11), 1950092. https://doi.org/10.1142/S012918311950092X

Dash, S. C., & Singh, N. (2019b). Influence of axial magnetic field on swirling flow and vortex breakdown zones in a cylindrical cavity with a rotating lid, *International Journal of Applied Mechanics*, 11(06), 1950054. https://doi.org/10.1142/S1758825119500546

Karthikeyan, S., Bhuvaneswari, M., Sivasankaran, S., & Rajan, S. (2016). Soret and dufour effects on mhd mixed convection heat and mass transfer of a stagnation point flow towards a vertical plate in a porous medium with chemical reaction, radiation and heat generation, *Journal of Applied Fluid Mechanics*, 9 (3), 1447-1455. https://doi.org/10.18869/acadpub.jafm.68.228.24135

Laouari, A., Mahfoud, B., & Hadjadj, A. (2021). Hydrodynamic instabilities in swirling flow under axial magnetic field. *European Journal of Mechanics-B/Fluids*, 85, 245-260. https://doi.org/10.1016/j.euromechflu.2020.08.006

Li, Y. R., Imaishi, N., Azami, T., & Hibiya, T. (2004). Three-dimensional oscillatory flow in a thin annular pool of silicon melt. *Journal of Crystal Growth*, 260, 28–42. https://doi.org/10.1016/j.jcrysgro.2003.08.017

Mahfoud, B., & Bessaïh, R. (2012a). Stability of swirling flows with heat transfer in a cylindrical enclosure with co/counter-rotating end disks under an axial magnetic field. *Numerical Heat Transfer*, Part A, 463-482 . https://doi.org/10.1080/10407782.2012.654461

Mahfoud, B. (2021a). Effects of an axial magnetic field on vortex breakdown and fluid layer. *Journal of Applied Fluid Mechanics*, 14, 1741–1753. https://doi.org/10.47176/jafm.14.06.32585

Mahfoud, B. (2021b). Magnetohydrodynamic effect on vortex breakdown zones in coaxial cylinders. *European Journal of Mechanics-B/Fluids*, 89, 445–457. https://doi.org/10.1016/j.euromechflu.2021.07.007 0997-7546

Mahfoud, B. (2022). Simulation of magnetic field effect on heat transfer enhancement of swirling nanofluid. *International Journal of Computational Materials Science and Engineering*, 11(4), 2250007. https://doi.org/10.1142/S2047684122500075

Mahfoud, B. (2023a). Effect of wall electrical conductivity on heat transfer enhancement of swirling nanofluid-flow. *Journal of Nanofluids*, 12, 418-428. https://doi.org/10.1166/jon.2023.1932

Mahfoud, B. (2023b). Enhancement heat transfer of swirling nanofluid using an electrical conducting. *Lid Journal of Thermophysics and Heat Transfer*, 37, 263-271. https://doi.org/10.2514/1. T6550

Mahfoud, B., & Bendjaghloli, A. (2018). Natural convection of a nanofluid in a conical container. *Journal of Thermal Engineering*, 4, 1713-1723. https://doi.org/10.18186/journal-of-thermal-engineering.367407

Mahfoud, B., & Mahfoud, Hibet. E. (2023). Behaviors of vortex breakdown in steady-state and oscillatory flow under an axial magnetic, *Researchgate.net/publication*. https://doi.org/10.13140/RG.2.2.14239.23200.

Mahfoud, B., & Moussaoui, M. (2023). Effects of buoyancy force and magnetic field on laminar vortex breakdown and fluid layers. *Journal of Thermal Engineering*, 9(1), 12–23. https://doi.org/10.18186/thermal.1232431

Mahfoud, B., & Bessaïh, R. (2012b). Oscillatory swirling flows in a cylindrical enclosure with co-/counter-rotating end disks submitted to a vertical temperature gradient. *Fluid Dynamics &MaterialsProcessing*, 2012, *8*(1), 126. https://doi.org/10.3970/fdmp.2011.008.001

Mahfoud, B., Bendjaghlouli, A., & Bessih, R. (2016). Magneto-hydrodynamic co-rotating flow in a vertical cylindrical container, *Numer. Heat Transfer*, 69(12,) 1051-1063. https://doi.org/10.1080/10407782.2015.1109383

Mahfoud, B., Laouari, A., Hadjadj, A., & Benhacine, H. (2019a). Counter-rotating flow in coaxial cylinders under an axial magnetic field. *European Journal of Mechanics-B/Fluids*, 78, 139-46. https://doi.org//10.1016/j.euromechflu.2019.06.009

Mahfoud, B., Benhacine, H., Laouari, A., & Bendjaghlouli, A. (2019b). Magnetohydrodynamic effect on flow structures between coaxial cylinders heated from below. *Journal of Thermophysics and Heat Transfer*, 34(2), 265–274. https://doi.org/10.2514/1.T5805

Mahfoud, B., & Bessih, R. (2016). Magnetohydrodynamic counter-rotating flow in a cylindrical cavity. *International Journal of Heat and Mass Transfer*, 93, 175–185. https://doi.org/10.1016/j.ijheatmasstransfer.2015.10.009

Malleswaran, A., & Sivasankaran, S. (2016). A Numerical simulation on Mhd mixed convection in a lid-driven cavity with corner heaters, *Journal of Applied Fluid Mechanics*, 9 (1), 311-319. https://doi.org/10.18869/acadpub.jafm.68.224.22903

Mihel, M., & Wingerath, K. (1987). Three-dimensional simulations of the Czochralski bulk flow in a stationary transverse field and in a vertical magnetic field: Effects on the asymmetry of the flow and temperature distribution in the Si melt. *Journal of Crystal Growth*, 82, 318–326. https://doi.org/10.1016/0022-0248(87)90320-4

Niranjana, H., Sivasankarana, S., & Bhuvaneswarib, M. (2017). Chemical reaction, Soret and Dufour effects on MHD mixed convection stagnation point ow with radiation and slip condition, *Scientia Iranica B*, 24(2), 698-706. https://doi.org/10.24200/sci.2017.4054

Okano, Y., Hatano, A., & Hirata, A. (1989). Natural and marangoni convections in a floating zone. *Journal of Chemical Engineering of Japan*, 22, 385– 388. https://doi.org/10.1252/jcej.22.385

Patankar, S. (1980). *Numerical Heat Transfer and Fluid Flow*. McGraw-Hill, New-York.

Rao, F., & Peng, L. (2017). Effect of axial magnetic field on thermocapillary convection with bidirectional temperature gradients in a shallow annular. *Crystal Research and Technology*. 1600342. https://doi.org/10.1002/crat.201600342

Sankar, M., Venkatachalappa, M., & Do, Y. (2011). Effect of magnetic field on the buoyancy and thermocapillary driven convection of an electrically conducting fluid in an annular enclosure. *International Journal of Heat & FluidFlow*, 32,402–412. https://doi.org/10.1016/j.ijheatfluidflow.2010.12.001

Sivasankaran, S., & Ching-Jenq, H. (2008). Effect of temperature dependent properties on MHD convection of water near its density maximum in a square cavity, *International Journal of Thermal Sciences*, 49 (9), 1184-1194. https://doi.org/10.1016/j.ijthermalsci.2007.10.001

Sivasankaran, S., Malleswaran, A., Lee, J., & Sundar, P. (2011). Hydro-magnetic combined convection in a lid-driven cavity with sinusoidal boundary conditions on both sidewalls, *International Journal of Heat and Mass Transfer*, 54(1-3), 512-525. https://doi.org/10.1016/j.ijheatmasstransfer.2010.09.018

Sivasankaran, S., Niranjan, H., & Bhuvaneswari, M. (2017). Chemical reaction, radiation and slip effects on MHD mixed convection stagnation-point flow in a porous medium with convective boundary condition, *International Journal of Numerical Methods for Heat & Fluid Flow*, 27(2), 454 -470. https://doi.org/10.1108/HFF-02-2016-0044

Slatni, Y., Messai, T., & Mahfoud, B. (2022). Numerical simulation of thermal behavior in a naturally ventilated greenhouse, *International Journal of Computational Materials Science and Engineering*, 11, 2150034. https://doi.org/10.1142/S2047684121500342

Voronkov, V. (1982). The mechanism of swirl defects formation in silicon. *Journal of Crystal Growth*, 59-3, 625-643. https://doi.org/10.1016/0022-0248(82)90386-4

Wang, C., Zhang, H., Wang, T. H., & Ciszek, T. F. (2003). A continuous Czochralski silicon crystal growth system. *Journal of Crystal Growth*, 250(1), 209-214. https://doi.org/10.1016/S0022-0248(02)02241-8

Wang, F., Pang, L., & Quan Zhuang, Z. (2014). Three-dimensional flow in a thin annular layer of silicon melts with bidirectional temperature gradients. *Crystal Research and Technology*, 49(10), 829–835. https://doi.org/10.1002/crat.201400212

Wang, F., Peng, L., Zhang, Q. Z., & Liu, J. (2015). Effect of horizontal temperature difference on Marangoni-thermocapillary convection in a shallow annular pool. *Acta Physica Sinica*, 14, 17–24. https://doi.org/10.7498/aps.64.140202